



**HAL**  
open science

## **Analytic treatment of nonparaxial full-Poincaré fields: singularity structure and trapping properties**

Rodrigo Gutiérrez–cuevas, Miguel Alonso

► **To cite this version:**

Rodrigo Gutiérrez–cuevas, Miguel Alonso. Analytic treatment of nonparaxial full-Poincaré fields: singularity structure and trapping properties. *Journal of Optics*, 2021, 23 (2), pp.024005. <10.1088/2040-8986/abe01f>. <hal-03363160>

**HAL Id: hal-03363160**

**<https://hal.science/hal-03363160v1>**

Submitted on 27 Feb 2022

HAL is a multi-disciplinary open access archive for the deposit and dissemination of scientific research documents, whether they are published or not. The documents may come from teaching and research institutions in France or abroad, or from public or private research centers.

L'archive ouverte pluridisciplinaire HAL, est destinée au dépôt et à la diffusion de documents scientifiques de niveau recherche, publiés ou non, émanant des établissements d'enseignement et de recherche français ou étrangers, des laboratoires publics ou privés.



Distributed under a Creative Commons CC BY-NC-ND 4.0 - Attribution - Non-commercial use - No Derivative Works - International License

# Analytic nonparaxial full-Poincaré fields: singularity structure and trapping properties

Rodrigo Gutiérrez-Cuevas<sup>1,\*</sup> and Miguel A. Alonso<sup>1,2,3,†</sup>

<sup>1</sup>*Aix Marseille Univ, CNRS, Centrale Marseille, Institut Fresnel, UMR 7249, 13397 Marseille Cedex 20, France*

<sup>2</sup>*The Institute of Optics, University of Rochester, Rochester, New York 14627, USA*

<sup>3</sup>*Center for Coherence and Quantum Optics, University of Rochester, Rochester, New York 14627, USA*

(Dated: January 9, 2021)

An analytic extension of the full-Poincaré beams to the nonparaxial regime is presented. Instead of the stereographic mapping used in the paraxial case, these full-Poincaré fields are defined in terms of a mapping from the polarization Poincaré sphere onto the sphere of plane-wave directions. It is shown that multipolar fields with complex arguments can be used to implement this mapping and provide closed-form expressions. The three-dimensional polarization singularities of the resulting fields are studied with the help of auxiliary fields presenting vortices at points where the polarization is circular or linear. Finally, the Mie scattering and trapping properties of the full-Poincaré fields are studied, both of which are greatly simplified by the choice of fields.

## I. Introduction

The study of structured light has seen significant growth in the last decades, leading to applications in numerous fields such as imaging, information transfer, and micromanipulation [1–3]. This is in large part due to the development of efficient and accessible methods for structuring light, such as the generation of phase singularities by Soskin and collaborators through diffraction holograms [4–6]. These methods have since evolved, and now allow shaping all of light’s degrees of freedom [7–10], including polarization [3, 11]. For example, the use of radially and azimuthally polarized light has expanded the control of optical traps [12], and the generally nonseparable nature of modal and polarization structure of light has proven useful for quantum information applications [13, 14].

Just like scalar fields can have phase singularities, nonuniformly polarized vector beams generally possess polarization singularities [15–18]. These structurally-stable features come in two types: C points, which are points of circular polarization where the direction of the major axis is ill-defined, and L points, which are points of linear polarization where handedness is ill-defined. Particular emphasis has been placed on the study of C points, since they trace lines in three-dimensional space, which can form closed loops and knots, even in the paraxial regime [19–23]. C points can be further classified according to the distribution of the polarization lines traced by the major axes of the surrounding polarization ellipses. There are three main types of C points: “lemon”, “star”, and “monstar”, where one, three, and an infinite number of polarization lines terminate, respectively. These types of C points are the ones that appear “in the wild”, i.e. in random fields [16, 17, 20]. However, higher-order singularities can be generated with purpose-

fully designed fields [18, 24–26]. Note that for the very restrictive case of purely linearly-polarized fields there is a third type of polarization singularity, V points [24], where the direction of linear polarization is not defined, e. g. at the axis of radially and azimuthally polarized fields. In this work we consider the more common case of fields in which the polarization ellipticity changes in space.

Full-Poincaré (FP) beams are examples of vector beams with nonuniform polarization distributions, which were introduced as a way to map all possible paraxial polarization states onto each transverse plane of a beam [27–29]. They can be expressed as the superposition of orthogonally-polarized Gaussian and vortex Laguerre-Gauss beams. At the waist plane this superposition can be written as

$$\mathbf{E} = E_0 \left( \cos \alpha \mathbf{v}_1 + \sin \alpha \frac{\rho}{w} e^{i\phi} \mathbf{v}_2 \right) e^{-\rho^2/w^2}, \quad (1)$$

where  $\mathbf{v}_1^\dagger \cdot \mathbf{v}_2 = 0$ ,  $\|\mathbf{v}_1\| = \|\mathbf{v}_2\| = 1$ ,  $w$  is the waist of the Gaussian,  $\alpha$  is the mixing angle controlling the ratio between the two polarization components,  $E_0$  is the amplitude of the field, and  $\rho$  and  $\phi$  are the polar coordinates. Fully polarized paraxial light is commonly described with the help of a Jones vector,

$$\mathbf{v}(\vartheta, \varphi) = \cos \frac{\vartheta}{2} e^{-i\varphi/2} \boldsymbol{\epsilon}_+ + \sin \frac{\vartheta}{2} e^{i\varphi/2} \boldsymbol{\epsilon}_-, \quad (2)$$

written here in terms of the circular polarization vectors  $\boldsymbol{\epsilon}_\pm = (\hat{\mathbf{x}} \pm i\hat{\mathbf{y}})/2^{1/2}$ . The angles  $\vartheta$  and  $\varphi$  are the polar and azimuthal coordinates on the Poincaré sphere (PS) as shown in Fig. 1. Comparing Eqs. (1) and (2), it can be seen that, geometrically, the polarization distribution of a FP beam is given by a stereographic projection of the PS onto the transverse plane mapping the polarization  $\mathbf{v}_1$  to the origin and  $\mathbf{v}_2$  to infinity. In particular, if  $\mathbf{v}_1$  and  $\mathbf{v}_2$  are chosen to be circular left and right polarization vectors then the resulting FP beam exhibits either a lemon or star C point polarization singularity at the origin. For a FP beam as in Eq. (1) the mapping is one-to-one; however, by changing the vortex charge and/or considering higher-order radial modes, the PS sphere can

\* rodrigo.gutierrez-cuevas@fresnel.fr

† miguel.alonso@fresnel.fr

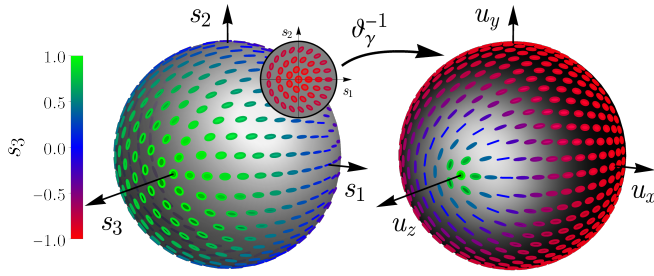


FIG. 1. Mapping of the PS (left) onto the SD (right) through the function  $\vartheta_\gamma^{-1}$  given in Eq. (6). The axes of the PS are the normalized Stokes parameters  $s_j$  and the inset shows the area around the south pole. The amplitude and polarization distribution of the plane-wave spectrum for the lemon FP field with  $k\zeta = 5$  and  $\delta = \pi/4$ , which determine the parameter  $\gamma$  of the mapping, are shown in the SD.

be mapped several times onto to transverse plane. These higher-order FP beams can also lead to higher-order polarization singularities [24, 25, 29]. Generalizations of FP beams into the nonparaxial regime have been proposed [27, 30, 31], but these are either not given by analytic expressions or are not defined in terms of a simple geometrical mapping allowing a direct extension to higher-order fields.

Here, it is shown that a geometrical mapping is possible in the nonparaxial regime between the PS and the sphere of directions. This is achieved by considering superpositions of simple multipoles evaluated at complex arguments [32, 33] leading to closed-form solutions of Maxwell's equations that reduce to LG beams in the paraxial regime [34–37]. It is shown that, for these fields, the transverse polarization distribution (which only takes into account the transverse components of the electric field) mimics that of the paraxial FP beams. Additionally, the full three-dimensional structure is examined with the help of auxiliary complex scalar and vector fields presenting phase vortices at points where the polarization is circular or linear. Lastly, the Mie scattering and trapping properties of the nonparaxial FP fields is studied.

## II. Definition of nonparaxial full-Poincaré fields

### A. Sphere-to-sphere mapping

An electromagnetic monochromatic field with wavenumber  $k$  propagating in free space can be written as a superposition of plane waves,

$$\mathbf{E}(\mathbf{r}) = \int_{4\pi} \mathbf{A}(\mathbf{u}) e^{ik\mathbf{u}\cdot\mathbf{r}} d\Omega, \quad (3)$$

where the unit vector  $\mathbf{u} = (\cos\phi \sin\theta, \sin\phi \sin\theta, \cos\theta)$  indicates the direction of propagation of each plane wave, parametrized here in terms of the polar and azimuthal angles  $\theta$  and  $\phi$ . The plane-wave spectrum  $\mathbf{A}(\mathbf{u})$ , which

is proportional to the far field, is a vector field defined over the sphere of directions (SD) for  $\mathbf{u}$ . The transversality condition implies that  $\mathbf{u} \cdot \mathbf{A}(\mathbf{u}) = 0$  so that  $\mathbf{A}$  is tangent to the surface of the SD and can be expressed in terms of a polarization basis conformed of a pair of orthogonal vectors  $\mathbf{V}_\mathbf{u}$  and  $\mathbf{u} \times \mathbf{V}_\mathbf{u}^\dagger$  satisfying  $\mathbf{u} \cdot \mathbf{V}_\mathbf{u} = 0$ . Locally, these vectors span a plane in which we can define a polarization state through the standard paraxial formulas. Therefore, we can generalize FP beams to the nonparaxial regime by means of the more natural mapping from the PS to the SD (see Fig. 1). This mapping is further motivated by the fact that, in the paraxial regime, only the small cap of the SD in the forward direction is occupied by the plane-wave spectrum, which then coincides with the 2D Fourier transform of the paraxial beam at the waist plane; for paraxial FP beams, this Fourier spectrum exhibits a polarization pattern similar to that in configuration space, so that the stereographic projection of the Poincaré sphere also applies to the plane-wave spectrum.

To implement this sphere-to-sphere mapping, we must use an appropriate polarization basis over the SD. A good option is  $\mathbf{V}_\mathbf{u}^{(\pm)} = \exp(i\pi/4)(\mathbf{u} \times \boldsymbol{\epsilon}_\pm \times \mathbf{u} \pm i\mathbf{u} \times \boldsymbol{\epsilon}_\pm)$  [36], which maps circular polarization according to parallel transport from the forward  $+\hat{\mathbf{z}}$  direction and is therefore consistent with the Richards-Wolf theory of focusing systems [35, 36, 38, 39]. These vectors are not normalized to unity; instead they satisfy  $\|\mathbf{V}_\mathbf{u}^{(\pm)}\| = \cos(\theta/2)$  and thus vanish at the  $-\hat{\mathbf{z}}$  direction, which is a degenerate singularity of this basis [35, 36, 40], chosen to be as distant as possible from the  $+\hat{\mathbf{z}}$  direction around which the plane-wave spectrum of directional fields concentrates.

These considerations raise, in turn, requirements on the mapping from the PS to the SD. This mapping must mimic the plane-wave spectrum of focused fields and hence allow the concentration of most polarization states within the forward-propagating hemisphere. By rewriting the Jones vector in the following form

$$\mathbf{v}(\vartheta, \varphi) = \frac{e^{-i\varphi/2}}{2 \cos \frac{\vartheta}{2}} \left[ (1 + \cos \vartheta) \boldsymbol{\epsilon}_+ + \sin \vartheta e^{i\varphi} \boldsymbol{\epsilon}_- \right], \quad (4)$$

we can see that one way to concentrate polarization states around the forward direction is to write the plane-wave spectrum for a lemon (+) or a star (−) FP field as

$$\mathbf{A}^{(\pm)}(\theta, \phi) = E_0 \left[ (1 + \cos \theta) \mathbf{V}_\mathbf{u}^{(\pm)} + \gamma \sin \theta e^{i\phi} \mathbf{V}_\mathbf{u}^{(\mp)} \right] f(\theta), \quad (5)$$

which has the same basic form as the Jones vector in Eq. (4) but changes the ratio of each polarization by the introduction of the parameter  $\gamma$ . This change of ratio defines the mapping

$$\vartheta_\gamma(\theta) = \frac{\pi}{2} - \tan^{-1} \left( \frac{1}{\gamma} \cot \theta + \frac{1 - \gamma^2}{2\gamma} \tan \frac{\theta}{2} \right), \quad (6)$$

between the PS and the SD. For the lemon FP field, when  $\gamma > 1$  the circle of linear polarization is moved

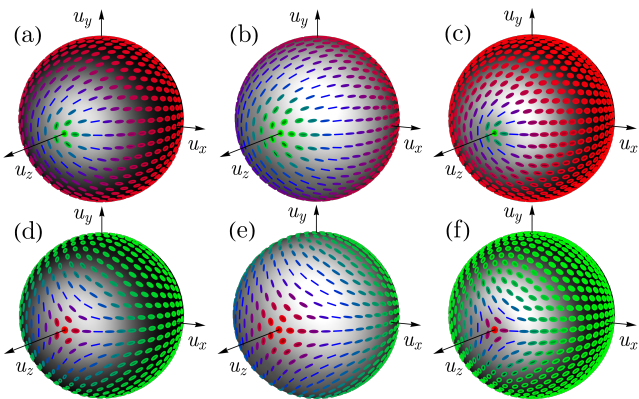


FIG. 2. Effect to the parameters  $\zeta$  and  $\delta$  on the plane-wave spectrum and its polarization distribution: for the (a-c) lemon and (d-f) star FP fields with (a,d)  $k\zeta = 5$  and  $\delta = \pi/4$ , (b,e)  $k\zeta = 1$  and  $\delta = \pi/4$ , and (c,f)  $k\zeta = 5$  and  $\delta = \pi/3$ .

into the forward-propagating hemisphere while leaving the left-circular polarization fixed at the south pole, as can be appreciated from Fig. 1 and two lemon C point singularities are created at the poles. For the star FP fields, the locations of right and left circular polarizations are reversed and two star C points are created at each pole. Note that the mapping defined by Eqs. (5) and (6) over the SD is analogous to the one enacted on the PS by a dichroic element [41].

### B. Plane-wave spectrum

Equation (5) allows concentrating most of the polarization structure into the forward-propagating hemisphere. The same type of concentration is then needed for the amplitudes of the plane waves through the function  $f(\theta)$ . Many such weight functions could be used but not all would lead to a simple analytic expression in configuration space. One option that provides both an analytic expression for the electric field through Eq. (3) and a continuous connection to the paraxial regime is  $f(\theta) = \exp(k\zeta \cos \theta)$  [42]. This real exponential can be interpreted as an imaginary shift  $z \rightarrow z - i\zeta$  in configuration space [32, 33]. Assuming a normalized plane wave spectrum according to  $\int \|\mathbf{A}\| d\Omega = |E_0|^2$ , the expression for the lemon and star FP fields in Eq. (5) can be rewritten as

$$\begin{aligned} \mathbf{A}^{(\pm)}(\mathbf{u}) &= \frac{E_0}{\sqrt{4\pi}} \left[ \alpha_r(\zeta) \cos \delta (1 + \cos \theta) \mathbf{V}_{\mathbf{u}}^{(\pm)} \right. \\ &\quad \left. - \alpha_v(\zeta) \sin \delta \sqrt{\frac{3}{2}} \sin \theta e^{i\phi} \mathbf{V}_{\mathbf{u}}^{(\mp)} \right] e^{k\zeta \cos \theta} \\ &= E_0 \left\{ \alpha_r(\zeta) \cos \delta \mathbf{V}_{\mathbf{u}}^{(\pm)} \left[ Y_{0,0}(\theta, \phi) + \frac{1}{\sqrt{3}} Y_{1,0}(\theta, \phi) \right] \right. \\ &\quad \left. - \alpha_v(\zeta) \sin \delta \mathbf{V}_{\mathbf{u}}^{(\mp)} Y_{1,1}(\theta, \phi) \right\} e^{k\zeta \cos \theta}, \end{aligned} \quad (7)$$

where  $\alpha_r$  and  $\alpha_v$  are normalization coefficients. In order to give a hint of how these expressions can be generalized to higher orders, the second form is written in terms of the spherical harmonics,

$$Y_{l,m}(\theta, \phi) = \sigma_m^m \sqrt{\frac{(2l+1)(l-m)!}{4\pi(l+m)!}} P_l^{(m)}(\cos \theta) e^{im\phi} \quad (8)$$

where  $\sigma_m = \text{sgn}(m + 1/2)$  and  $P_l^{(m)}$  is the associated Legendre polynomial. (Note that other FP fields can be generated by replacing the two polarization vectors  $\mathbf{V}_{\mathbf{u}}^{(\pm)}$  with two orthogonal linear combinations of these vectors.) The parameter  $\gamma$  introduced in Eq. (6) becomes a function of  $\delta$  and  $\zeta$ ,

$$\gamma(\delta, \zeta) = \sqrt{\frac{3}{2}} \frac{\alpha_v(\zeta)}{\alpha_r(\zeta)} \tan \delta. \quad (9)$$

The effect of  $\zeta$  and  $\delta$  on the amplitude and polarization distribution of  $\mathbf{A}$  is shown in Fig. 2. The directionality parameter  $\zeta$ , which corresponds to the Rayleigh range in the paraxial limit, has a similar effect on both the amplitude and the polarization distribution: for increasing  $\zeta$  they become more concentrated around the  $+\hat{\mathbf{z}}$  direction, whereas the parameter  $\delta$  only controls the ratio of the two orthogonal components thus allowing changing the polarization distribution independently from the focusing properties.

In the paraxial limit, i.e. for  $k\zeta \gg 1$ , the plane-wave spectrum in Eq. (7) expressed as an exponential weight times the superposition of  $Y_{0,0}$  and  $Y_{1,1}$  indeed corresponds to the superposition of a Gaussian and the lowest-order Laguerre-Gauss mode with a vortex [as the one in Eq. (1)]. However, note that the term  $Y_{1,0}$  is needed to achieve the one-to-one mapping between the spheres. This term alone tends in the paraxial limit to an LG beam with a higher-order radial structure, which is not present in the original FP beams (see Eq. (1)) [32, 33, 35, 36]. This extra term is a nonparaxial correction whose relative amplitude vanishes in the paraxial limit. For  $k\zeta > 3$ , the relative weight of this extra term is less than 5%, hinting that its effect is only significant for considerably focused fields. Therefore, the FP fields defined here do reduce to the standard FP beams in the paraxial limit.

### C. Configuration space

The advantage of using imaginary shifts in  $z$  is the resulting simplicity of the expressions in configuration space, as opposed to the most common approach of using the Richards-Wolf theory which usually requires numerical integration [30, 31, 38, 39]. Using the relation

$$\Lambda_{l,m}(\mathbf{r}) = \int_{4\pi} Y_{l,m}(\mathbf{u}) e^{ik\mathbf{u}\cdot\mathbf{r}} d\Omega, \quad (10)$$

satisfied between the spherical harmonics and the scalar multipoles,

$$\Lambda_{l,m}(\mathbf{r}) = 4\pi i^l j_l(kr) Y_{l,m}(\theta_r, \phi_r), \quad (11)$$

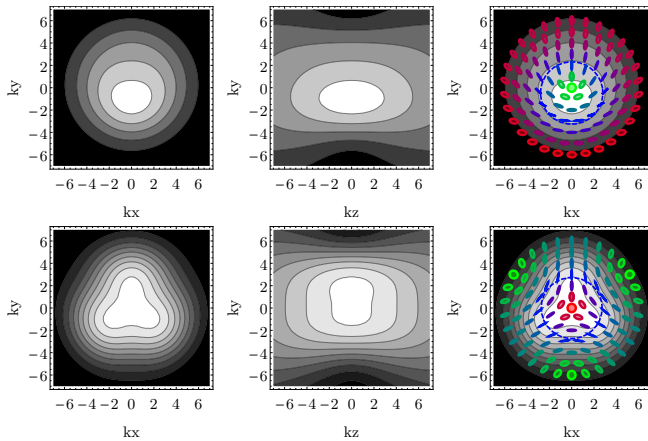


FIG. 3. Amplitude distribution along the (first column)  $x-y$  and (second column)  $y-z$  planes and (third column) the intensity along the  $x-y$  plane with the transverse polarization distribution overlaid, with the dashed blue line corresponding to the L line, for the (first row) lemon and (second row) star with  $k\zeta = 5$  and  $\delta = \pi/4$ .

where  $j_l$  are the spherical Bessel functions, and the fact that the polarization operators in configuration space are obtained by performing the substitution  $\mathbf{u} \rightarrow \nabla/ik$ , the FP fields in configuration space can be written as

$$\mathbf{E}^{(\pm)}(\mathbf{r}; \zeta) = E_0 \left\{ \alpha_r(\zeta) \cos \delta \mathbf{V}_r^{(\pm)} \left[ \Lambda_{0,0}(\mathbf{r} - i\zeta\hat{\mathbf{z}}) + \frac{1}{\sqrt{3}} \Lambda_{1,0}(\mathbf{r} - i\zeta\hat{\mathbf{z}}) \right] - \alpha_v(\zeta) \sin \delta \mathbf{V}_r^{(\mp)} \Lambda_{1,1}(\mathbf{r} - i\zeta\hat{\mathbf{z}}) \right\}, \quad (12)$$

where

$$\mathbf{V}_r^{(\pm)} = \frac{1}{k^2} \boldsymbol{\epsilon}_{\pm} \times \nabla \times \nabla \mp \frac{1}{k} \boldsymbol{\epsilon}_{\pm} \times \nabla. \quad (13)$$

Note that the derivatives can be computed analytically using the recurrence relations for spherical Bessel functions and associated Legendre polynomials, thus providing a closed-form expression for the fields in configuration space. As shown in Fig. 3, the amplitude distribution depends on the polarization distribution. For both the lemon and star FP fields the amplitude distribution is no longer circularly symmetric but carries a distinct signature from the polarization distribution in the SD. This coupling between amplitude and polarization has the same origin as the spin-orbit coupling [43].

Figure 3 also shows the transverse polarization distribution (which consider only the  $x$  and  $y$  components of the field) at the focal plane. This distribution resembles that of the paraxial FP beams and the one encoded in the plane-wave spectrum. Nonetheless, focusing causes some small changes such as a slight deformation of the L line in the lemon FP due to the asymmetric shape. It should also be noticed that the polarization pattern at the focal

plane is rotated by  $45^\circ$  with respect to the one encoded in the plane-wave spectrum due to the difference in Gouy phase acquired between the two polarization components as they propagate from the focal plane to the far field [27].

### III. True polarization singularities

#### A. Transverse VS true polarization singularities

The transverse polarization of electromagnetic fields exhibits an analogous behavior to the polarization of paraxial fields since it only takes into account two field components. In particular, upon propagation, transverse C singularities trace three-dimensional lines while L singularities are distributed across surfaces. This fact can be understood from the number of constraints required to obtain each type of singularity. C point singularities are formed when the real and imaginary parts of the electric field vector are orthogonal and have equal norm. These two constraints restrict the C singularities to lines in space. L points, on the other hand, are formed when the phase difference between the two components is zero modulo  $\pi$ . This single constraint restrict L points to surfaces in space.

In the nonparaxial regime, the longitudinal component becomes non-negligible and thus must be taken into account for a complete description. This extra component allows the polarization ellipse to have an arbitrary 3D orientation. The true circular and linear polarization singularities, denoted respectively by  $C^T$  and  $L^T$ , take all three components into account [15]. Both these singularities behave similarly, tracing lines across space, due to the number of constraints needed to define them: for a  $C^T$  point the real and imaginary parts of the electric field must be orthogonal and of equal norm, as in the transverse case; for  $L^T$  points, the phase difference between the three components must vanish modulo  $\pi$ , hence imposing also two constraints.

The dimensionality of transverse (or paraxial) and true polarization singularities can also be understood from the corresponding geometrical representations of polarization. The paraxial or transverse polarization can be represented as a point on the surface of the PS. Circular polarization corresponds to isolated points (the poles), while linear polarization spans a line (the equator). The prescription of three-dimensional polarization requires instead two points on the surface of a unit sphere rather than one [44, 45], and the limiting cases of linear and circular polarization correspond to these two coinciding or being antipodal, respectively, both situations imposing the same number of constraints.

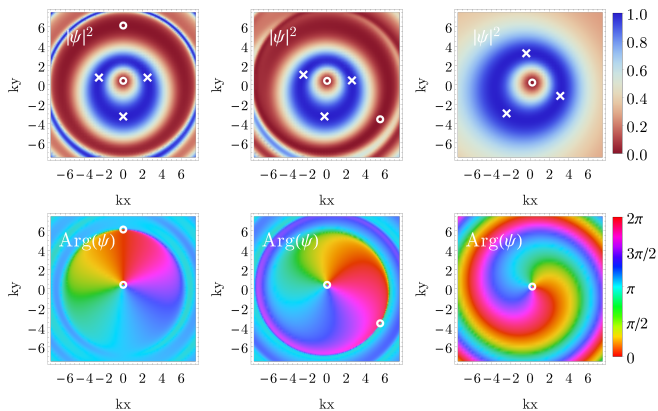


FIG. 4. Modulus squared (top) and argument (bottom) of the field  $\psi$  for the lemon FP field with  $k\zeta = 5$  and  $\delta = \pi/4$  at (from left to right)  $kz = 0, .5$  and  $1$ . The  $C^T$  points, which correspond to the zeros, are marked with circles and the  $L^T$  points, which correspond to the maximum value of one, are marked with crosses.

### B. True C point singularities

The electric spin density vector is defined as

$$\mathbf{S} = \frac{\text{Im}(\mathbf{E}^* \times \mathbf{E})}{\|\mathbf{E}\|^2}, \quad (14)$$

which points along the normal of the polarization ellipse and whose length determines the ellipticity. The norm of this vector is unity at  $C^T$  points and zero at  $L^T$  points. Another relevant quantity is the complex scalar field,

$$\psi = \frac{\mathbf{E} \cdot \mathbf{E}}{\|\mathbf{E}\|^2}, \quad (15)$$

which vanishes at  $C^T$  points where it exhibits phase singularities. The vortices of  $\psi$  greatly simplify the identification and tracking of  $C^T$  lines across space [16, 21, 46, 47]. These two quantities are related via

$$\|\mathbf{S}\|^2 = 1 - |\psi|^2. \quad (16)$$

Figures 4 and 5 show the modulus squared and phase of the field  $\psi$  for the lemon and star FP fields, respectively. Both fields have a  $C^T$  point near or at the transverse C point (which lies at the origin); for the lemon FP field it is translated slightly along the positive  $y$  axis due to the field's asymmetry while for the star FP field it is exactly at the origin. Both fields present other  $C^T$  points at regions where the fields becomes negligible.

### C. True L point singularities

$L^T$  points correspond to the zeros of the electric spin field. Nonetheless, it is possible to define a complex vector field with a role somewhat analogous to that of the

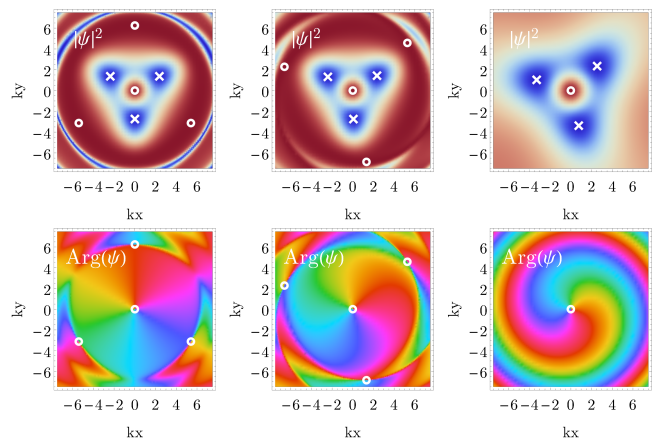


FIG. 5. Modulus squared (top) and argument (bottom) of the field  $\psi$  for the star FP field with  $k\zeta = 5$  and  $\delta = \pi/4$  at (from left to right)  $kz = 0, .5$  and  $1$ . The  $C^T$  points, which correspond to the zeros, are marked with circles and the  $L^T$  points, which correspond to the maximum value of one, are marked with crosses. These plots use the same color coding as the ones in Fig. 4.

field  $\psi$ , whose vortices facilitate tracking the  $L^T$  lines:

$$\boldsymbol{\xi} = \frac{1}{\sqrt{2}}(S_z - iS_y, S_x - iS_z, S_y - iS_x), \quad (17)$$

which vanishes where  $\mathbf{S}$  does, since it satisfies  $\|\boldsymbol{\xi}\| = \|\mathbf{S}\|$ . The components of this field can be written in terms of the electric field as

$$\xi_x = \frac{\sqrt{2}}{\|\mathbf{E}\|^2} [\text{Im}(E_x^* E_y) + i \text{Im}(E_x^* E_z)], \quad (18a)$$

$$\xi_y = \frac{\sqrt{2}}{\|\mathbf{E}\|^2} [\text{Im}(E_y^* E_z) + i \text{Im}(E_y^* E_x)], \quad (18b)$$

$$\xi_z = \frac{\sqrt{2}}{\|\mathbf{E}\|^2} [\text{Im}(E_z^* E_x) + i \text{Im}(E_z^* E_y)]. \quad (18c)$$

These expressions show that a given component  $\xi_j$  is zero if one of two conditions is met; either the corresponding electric field component  $E_j$  is zero or it is in phase or  $\pi$  out of phase with the other two components. The latter indicates the presence of a  $L^T$  point while the former is a pathological case which can be a  $L^T$  point if any of the other components of the field  $\boldsymbol{\xi}$  vanish. This definition is analogous to the one used to introduce the Stokes fields given by complex combinations of the Stokes parameters providing a simple way to identify polarization singularities in paraxial fields [26, 48, 49].

Figure 6 shows the argument of each component of the field  $\boldsymbol{\xi}$  for the lemon and star FP fields presenting different possible behaviors. The points marked with a cross indicate the presence of an  $L^T$  point and they correspond to zeros for all three components of  $\boldsymbol{\xi}$ . These also corresponds to the maxima of  $|\psi|$  shown in Figs. 4 and 5. Other vortices that do not correspond to  $L^T$  points can be seen in Fig. 6; these are points where the corresponding

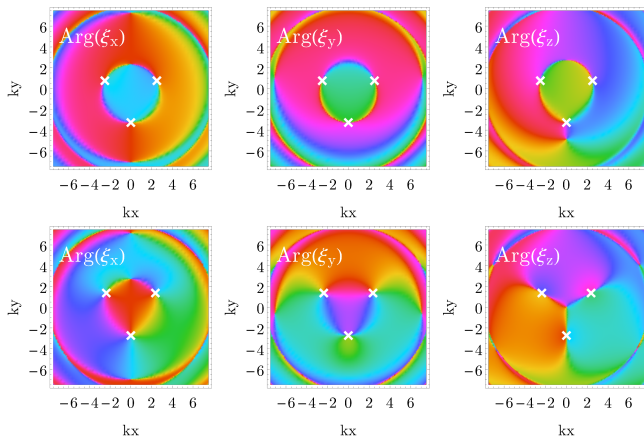


FIG. 6. Argument of the components of the field  $\xi$  for the lemon (top) and star (bottom) FP fields with  $k\zeta = 5$  and  $\delta = \pi/4$  with the  $L^T$  points marked by crosses. These plots use the same color coding as the one used in Fig. 4 for the argument of  $\psi$ .

component of the electric field is zero but the remaining two are not in phase or  $\pi$  out of phase, as evidenced by the lack of vortices for the other components of  $\xi$  at that location. Note that both FP fields no longer have a line of linear polarization across the transverse plane but rather a set of three  $L^T$  points, which are equally distributed azimuthally for the star FP field but not for the lemon FP field.

#### D. True polarization lines

Upon propagation, the  $C^T$  and  $L^T$  points form lines that can either remain open or form closed loops. Figure 7 shows these trajectories, which have been found numerically, along with transverse cuts of the amplitude of the field. For the lemon FP field all the singularities rotate around the origin under propagation, and two of the  $L^T$  points merge to form an unknotted closed  $L^T$  loop, an unknot. This loop becomes smaller/larger for fields with smaller/larger  $\zeta$  (more/less focused). The  $C^T$  line near the  $z$  axis turns around it and approaches it asymptotically away from the focal region. For the star FP field, on the other hand, the singularities rotate around the origin but remain open since the threefold symmetry prevents any two of them from merging, and the central  $C^T$  line coincides exactly with the  $z$  axis. For both FP fields, the  $C^T$  points that are further from the origin spiral out away from the focal plane moving further into regions where the fields are negligible (Figs. 4 and 5) and are thus not shown in Fig. 7. Note that  $L^T$  points always coincide with transverse L points (but not conversely), as opposed to  $C^T$  points. This confines  $L^T$  lines to the surfaces traced by the transverse L points. These L surfaces need to be topologically different from a cylinder in order to support knotted or linked  $L^T$  lines. However,

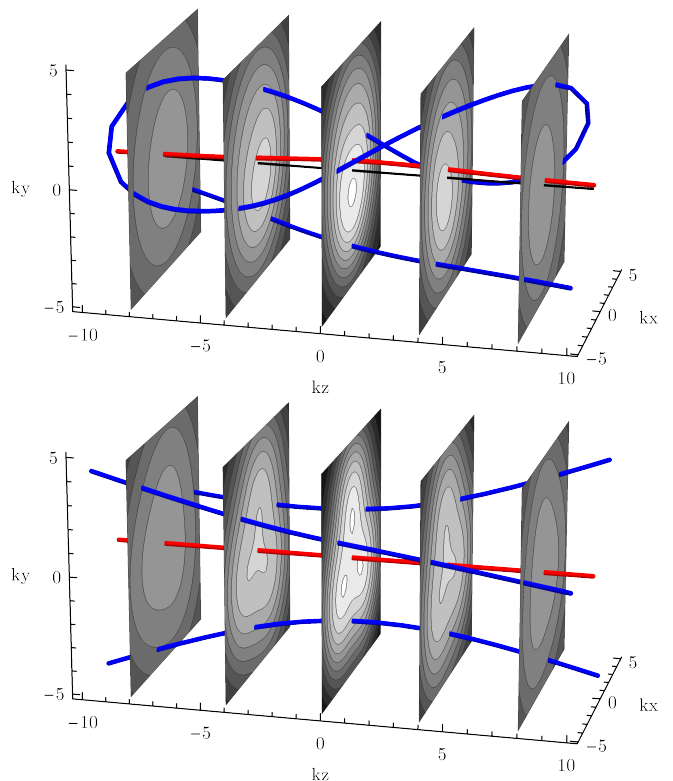


FIG. 7. Trajectories of the  $L^T$  (blue) and  $C^T$  (red) points for the lemon (top) and star (bottom) FP fields with  $k\zeta = 5$  and  $\delta = \pi/4$ .

for the FP fields studied here, the L surfaces are topologically equivalent to cylinders and can therefore support only open lines and unknots.

#### IV. Mie scattering of FP fields

An advantage of the simple form of the FP fields defined here is that their multipolar decomposition can be computed analytically given any relative position between the focus of the multipolar basis and that of the FP fields. Therefore, the FP fields lend themselves to an analytic treatment of their scattering by a spherical particle, albeit with an infinite sum, from which the induced forces and torques can be computed [37, 50, 51] without recurring to Rayleigh's approximation [39, 52]. Figure 8 shows the total field after being scattered by a spherical particle of radius  $kR = 3$  and refractive index  $\nu_0 = 1.3 + 10^{-4}i$  in free space, for both lemon and star FP fields. Note that the scattering changes significantly the intensity profile of the fields, but not the polarization distribution which is topologically stable. This can be appreciated in Fig. 8 where the polarization distribution is deformed but the lemon and star C points are still present.

Having solved the scattering problem, the forces and torques induced on the scatterer can be easily computed

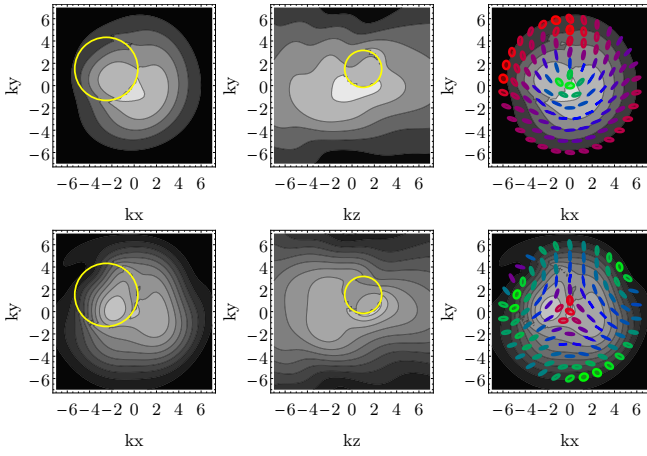


FIG. 8. Amplitude distribution along the (first column)  $x-y$  and (second column)  $y-z$  planes and (third column) the intensity along the  $x-y$  plane with the transverse polarization distribution overlaid for the total field generated by the scattering of the lemon (first row) and star (second row) full-Poincaré fields with  $k\zeta = 5$  and  $\delta = \pi/4$ . The scattering particle is a spherical particle of index of refraction  $\nu_0 = 1.3 + 10^{-4}i$  and radius  $kR = 3$  located at  $kr_p = (-2.5, 1.5, 1)$ . The yellow circles show the transverse cut of the sphere by the corresponding plane.

[37, 53]. Figure 9 shows the variations of the  $y$  component of the force and the  $z$  component of the torque along the  $y$  axis for the lemon FP field. Due to the field's asymmetric intensity distribution, the zero point of lateral force is offset to the negative  $y$  values for smaller particles. However, surprisingly, for larger particles this zero force point is shifted to the positive  $y$  values. Both shifts become more pronounced for particles with a higher refractive index. Another interesting feature is that the  $z$  component of the torque can take negative values at the edges of the focus even if the total angular momentum of the surrounding vortex field is zero due to its polarization opposite to the vortex charge.

Given the symmetric shape of the star FP field, the point of zero transverse force is always located at the origin, as shown in Fig. 10. This allows on-axis trapping if the particle properties are chosen correctly. Trapping in three directions is only possible if the  $z$  component of the force also presents a zero point along the  $z$  axis with negative slope. Figure 11 shows that, as a general rule, it is easier to trap smaller particles with a lower index of refraction. The trapping location is located after the focus of the field where the gradient force balances the radiation pressure. The presence and location of a stable point also depends on the degree of focusing of the field: a field that is more focused produces a greater intensity gradient closer to the focal region thus increasing its trapping capabilities, as shown in Fig. 12. These observations are in line with intuition.

The torque induced by the star FP field along the  $z$  axis only has a  $z$  component which is highly dependent

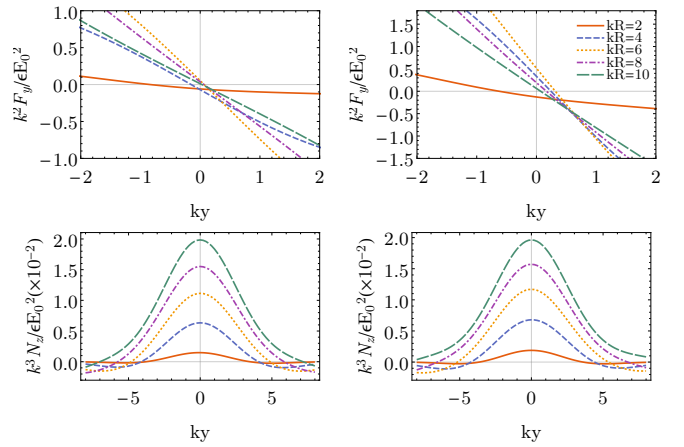


FIG. 9. Variation of the  $y$  component of the force (first row) and the  $z$  component of the torque (second row) along the  $y$  axis for a lemon FB field ( $k\zeta = 10$  and  $\delta = \pi/4$ ) on a spherical particles with varying size and relative index of refraction  $\nu_0 = 1.1 + 10^{-4}i$  (first column) and  $\nu_0 = 1.3 + 10^{-4}i$  (second column).

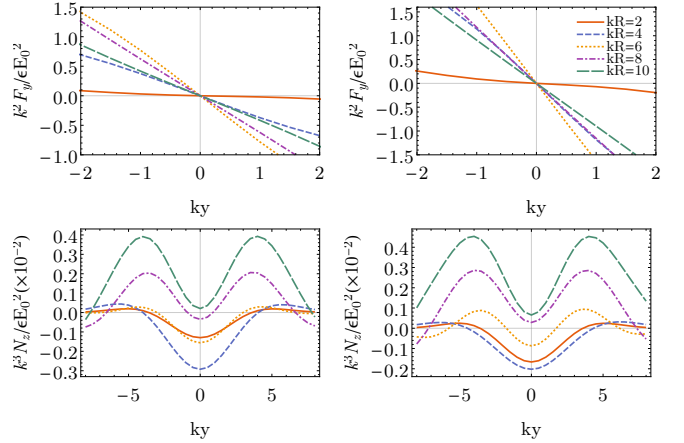


FIG. 10. Variation of the  $y$  component of the force (first row) and the  $z$  component of the torque (second row) along the  $y$  axis for a star FB field ( $k\zeta = 10$  and  $\delta = \pi/4$ ) on a spherical particles with varying size and relative index of refraction  $\nu_0 = 1.1 + 10^{-4}i$  (first column) and  $\nu_0 = 1.3 + 10^{-4}i$  (second column).

on the size of the scattering particle (see Fig. 11). This can be understood by the fact that the size of the particle dictates which parts of the field interact with it: If the particle is small then it only interacts with the inner part of the field which mainly carries left-circularly polarized light generating a negative torque; on the other hand, if the particle is large then it is affected by the vortex in which the orbital and spin angular momentum couple constructively in the opposite sense than the angular momentum of the inner part of field. Therefore, the  $z$  component of the induced torque goes from being negative for smaller particles to being positive for larger particle. Alternatively, if the field is more focused then the region

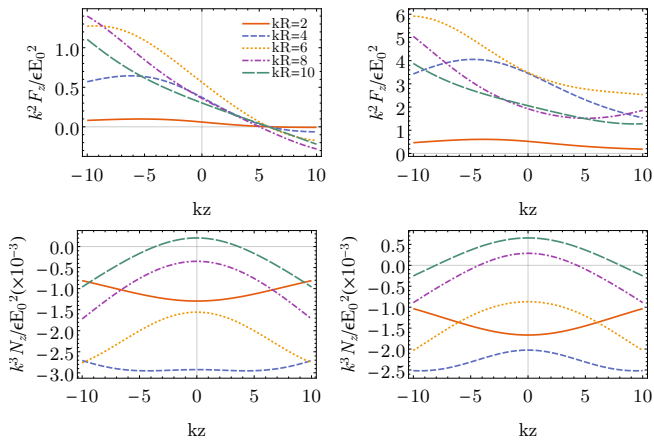


FIG. 11. Variations of the  $z$  components of the force (first row) and torque (second row) along the  $z$  axis for a star FB field ( $k\zeta = 10$  and  $\delta = \pi/4$ ) on a spherical particles with varying size and relative index of refraction  $\nu_0 = 1.1 + 10^{-4}i$  (first column) and  $\nu_0 = 1.3 + 10^{-4}i$  (second column).

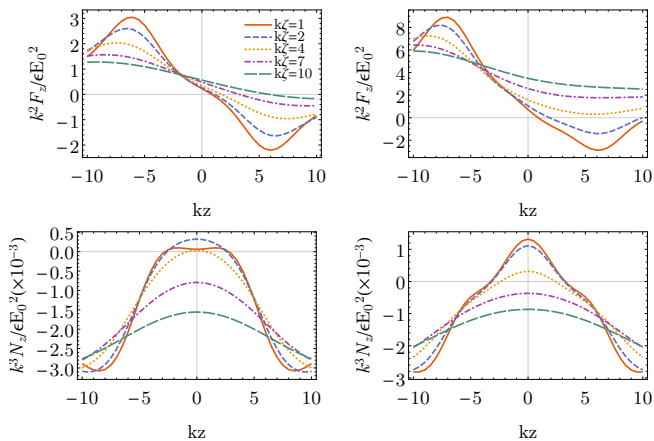


FIG. 12. Variations of the  $z$  components of the force (first row) and torque (second row) along the  $z$  axis for a star FB field with varying degree of focusing  $k\zeta$  ( $\delta = \pi/4$ ) on a spherical particle of radius  $kR = 6$  and relative index of refraction  $\nu_0 = 1.1 + 10^{-4}i$  (first column) and  $\nu_0 = 1.3 + 10^{-4}i$  (second column).

of left circular polarization shrinks, and thus increases the effect of the outer region of the field on smaller particles. The behavior of the induced torque as the focusing properties are changed is shown in Fig. 12 where its sign changes as the field is more focused. The parameter  $\delta$ , controlling the ratio between the two orthogonal polarization components, can also be tuned to obtain a desired effect. As already mentioned, this parameter changes the spread of the polarization distribution without changing the focusing properties of the field. This effect allows the control of the induced torque without affecting the trapping properties of the field, as shown in Fig. 13. It can then be used to twist the trapped particle by generating a torque that changes sign on each side of the trapping

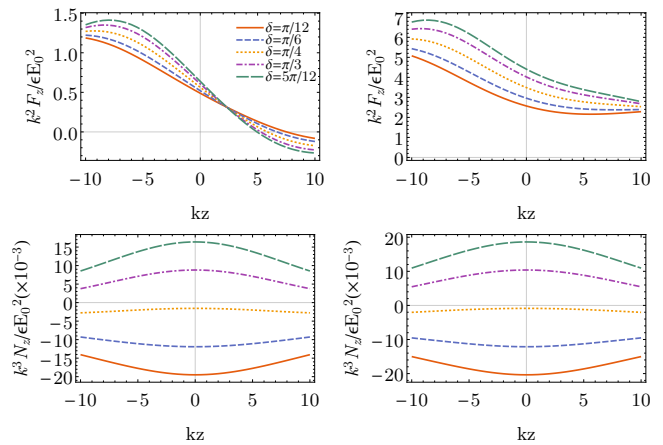


FIG. 13. Variations of the  $z$  components of the force (first row) and torque (second row) along the  $z$  axis for a star FB field with  $k\zeta = 10$  and varying ratio  $\delta$  on a spherical particle of radius  $kR = 6$  and relative index of refraction  $\nu_0 = 1.1 + 10^{-4}i$  (first column) and  $\nu_0 = 1.3 + 10^{-4}i$  (second column).

location.

## V. Concluding remarks

In the paraxial regime FP beams are defined through the stereographic mapping of the PS onto the transverse plane. However, they can equivalently be defined through a mapping from the PS onto the Fourier plane. This alternative view was exploited here to define nonparaxial FP fields through a mapping of the PS onto the SD, which is the nonparaxial extension of the Fourier plane for monochromatic fields. The mappings of polarization and amplitude were chosen so that the resulting fields had simple analytic expressions in terms of vector multipoles evaluated at complex arguments. It was shown that the transverse polarization has the same generic structure as of the paraxial FP beams.

The true polarization singularities, obtained by taking into account the three-dimensional nature of polarization, were studied with the help of the auxiliary fields  $\psi$  and  $\xi$ . The vector field  $\xi$  was introduced to aid in the identification of  $L^T$  points since it exhibits phase vortices in its components at  $L^T$  points. Therefore, it plays an analogous role to that of the field  $\psi$  for  $C^T$  points. These true singularities trace lines across space that either remain open or form closed loops.

While the original FP beams were introduced as a way to map all paraxial polarization states into the transverse plane, in the nonparaxial case it becomes impossible for a monochromatic field to span all possible three-dimensional polarization states. This is a simple consequence of the difference in dimensionality between the polarization space and physical space; the former is a four-dimensional manifold (the product of two spheres [44, 45]) while the latter is the three-dimensional Eu-

clidean space.

Several generalizations to this work are possible. One would be the extension of the sphere-to-sphere mapping to include higher order (radial and azimuthal) FP fields by increasing the number of cycles in the polar and azimuthal angles. This would involve replacing the spherical harmonics in Eq. (7) by higher-order ones, so that the field can still be expressed analytically in terms of multipoles. Also, other polarization singularities could

be considered, such as the monstar [54] or asymmetric structures [55]. Finally, an interesting alternative would be to consider other forms of the function  $f(\theta)$  introduced in Eq. (5) to generate the sphere-to-sphere mapping. One possibility is to use combinations of real exponentials leading to sums of CF fields with different values of the parameter  $\zeta$ , as in a type of basis function introduced recently [36, 56, 57].

- 
- [1] H. Rubinsztein-Dunlop, A. Forbes, M. V. Berry, M. R. Dennis, D. L. Andrews, M. Mansuripur, C. Denz, C. Alpmann, P. Banzer, T. Bauer, E. Karimi, L. Marrucci, M. Padgett, M. Ritsch-Marté, N. M. Litchinitser, N. P. Bigelow, C. Rosales-Guzmán, A. Belmonte, J. P. Torres, T. W. Neely, M. Baker, R. Gordon, A. B. Stilgoe, J. Romero, A. G. White, R. Fickler, A. E. Willner, G. Xie, B. McMorran, and A. M. Weiner, *J. Opt.* **19**, 013001 (2017).
- [2] G. J. Gbur, *Singular Optics* (CRC Press, 2016).
- [3] C. Rosales-Guzmán, B. Ndagano, and A. Forbes, *J. Opt.* **20**, 123001 (2018).
- [4] V. Y. Bazhenov, M. V. Vasnetsov, and M. S. Soskin, *Jetp. Lett.* **52**, 429 (1990).
- [5] N. R. Heckenberg, R. McDuff, C. P. Smith, and A. G. White, *Optics Letters* **17**, 221 (1992).
- [6] M. Beijersbergen, R. Coerwinkel, M. Kristensen, and J. Woerdman, *Optics Communications* **112**, 321 (1994).
- [7] V. Arrizón, U. Ruiz, R. Carrada, and L. A. González, *J. Opt. Soc. Am. A* **24**, 3500 (2007).
- [8] D. Naidoo, F. S. Roux, A. Dudley, I. Litvin, B. Piccirillo, L. Marrucci, and A. Forbes, *Nat. Photonics* **10**, 327 (2016).
- [9] A. Rubano, F. Cardano, B. Piccirillo, and L. Marrucci, *Journal of the Optical Society of America B* **36**, D70 (2019).
- [10] C. Maurer, A. Jesacher, S. Fürhapter, S. Bernet, and M. Ritsch-Marté, *New Journal of Physics* **9**, 78 (2007).
- [11] U. Levy, Y. Silberberg, and N. Davidson, *Adv. Opt. Photonics* **11**, 828 (2019).
- [12] T. A. Nieminen, N. R. Heckenberg, and H. Rubinsztein-Dunlop, *Opt. Lett.* **33**, 122 (2008).
- [13] L. Neves, G. Lima, A. Delgado, and C. Saavedra, *Physical Review A* **80** (2009), 10.1103/physreva.80.042322.
- [14] A. Forbes and I. Nape, *AVS Quantum Science* **1**, 011701 (2019).
- [15] J. F. Nye and J. V. Hajnal, *Proceedings of the Royal Society of London. A. Mathematical and Physical Sciences* **409**, 21 (1987).
- [16] M. Berry and M. Dennis, *Proceedings of the Royal Society of London. Series A: Mathematical, Physical and Engineering Sciences* **457**, 141 (2001).
- [17] M. Dennis, *Opt. Commun.* **213**, 201 (2002).
- [18] G. Milione, H. I. Sztul, D. A. Nolan, and R. R. Alfano, *Phys. Rev. Lett.* **107**, 053601 (2011).
- [19] K. O'Holleran, M. R. Dennis, F. Flossmann, and M. J. Padgett, *Physical Review Letters* **100**, 053902 (2008).
- [20] F. Flossmann, K. O'Holleran, M. R. Dennis, and M. J. Padgett, *Phys. Rev. Lett.* **100**, 203902 (2008).
- [21] K. O'Holleran, M. R. Dennis, and M. J. Padgett, *Physical Review Letters* **102**, 143902 (2009).
- [22] H. Larocque, D. Sugic, D. Mortimer, A. J. Taylor, R. Fickler, R. W. Boyd, M. R. Dennis, and E. Karimi, *Nature Physics* **14**, 1079 (2018).
- [23] D. Sugic and M. R. Dennis, *Journal of the Optical Society of America A* **35**, 1987 (2018).
- [24] I. Freund, *Opt. Commun.* **201**, 251 (2002).
- [25] E. Otte, C. Alpmann, and C. Denz, *Journal of Optics* **18**, 074012 (2016).
- [26] G. Arora, Ruchi, and P. Senthilkumaran, *Optics Letters* **44**, 5638 (2019).
- [27] A. M. Beckley, T. G. Brown, and M. A. Alonso, *Opt. Express* **18**, 10777 (2010).
- [28] A. M. Beckley, T. G. Brown, and M. A. Alonso, *Opt. Express* **20**, 9357 (2012).
- [29] E. J. Galvez, S. Khadka, W. H. Schubert, and S. Nomoto, *Applied Optics* **51**, 2925 (2012).
- [30] W. Zhu, V. Shvedov, W. She, and W. Krolikowski, *Opt. Express* **23**, 34029 (2015).
- [31] P. Yu, Y. Liu, Z. Wang, Y. Li, and L. Gong, *Ann. Phys.* **532**, 2000110 (2020).
- [32] M. V. Berry, *J. Phys. A: Math. Gen.* **27**, L391 (1994).
- [33] C. J. R. Sheppard and S. Saghaei, *Phys. Rev. A* **57**, 2971 (1998).
- [34] N. J. Moore and M. A. Alonso, *J. Opt. Soc. Am. A* **26**, 1754 (2009).
- [35] N. J. Moore and M. A. Alonso, *J. Opt. Soc. Am. A* **26**, 2211 (2009).
- [36] R. Gutiérrez-Cuevas and M. A. Alonso, *Opt. Express* **25**, 14856 (2017).
- [37] R. Gutiérrez-Cuevas, N. J. Moore, and M. A. Alonso, *Phys. Rev. A* **97**, 053848 (2018).
- [38] B. Richards and E. Wolf, *Proc. R. Soc. Lond. A* **253**, 358 (1959).
- [39] L. Novotny and B. Hecht, *Principles of Nano-Optics* (Cambridge University Press, 2006).
- [40] W. Chen, Y. Chen, and W. Liu, *Phys. Rev. Lett.* **122** (2019), 10.1103/physrevlett.122.153907.
- [41] H. Kubo and R. Nagata, *Journal of the Optical Society of America* **73**, 1719 (1983).
- [42] S. R. Jammalamadaka and A. Sengupta, *Topics In Circular Statistics-vol 5* (World Scientific Publishing Co Pte Ltd, 2001).
- [43] K. Y. Bliokh, M. A. Alonso, E. A. Ostrovskaya, and A. Aiello, *Phys. Rev. A* **82**, 063825 (2010).
- [44] J. H. Hannay, *J. Mod. Opt.* **45**, 1001 (1998).
- [45] K. Y. Bliokh, M. A. Alonso, and M. R. Dennis, *Rep. Prog. Phys.* **82**, 122401 (2019).
- [46] C. L. Phillips, T. Peterka, D. Karpeyev, and A. Glatz, *Physical Review E* **91** (2015), 10.1103/phys-

- [reve.91.023311](#).
- [47] A. J. Taylor and M. R. Dennis, *Nat. Commun.* **7**, 12346 (2016).
  - [48] I. Freund, *Optics Letters* **26**, 1996 (2001).
  - [49] I. Freund, A. I. Mokhun, M. S. Soskin, O. V. Angelsky, and I. I. Mokhun, *Optics Letters* **27**, 545 (2002).
  - [50] N. J. Moore and M. A. Alonso, *Opt. Express* **16**, 5926 (2008).
  - [51] N. J. Moore and M. A. Alonso, *J. Opt. Soc. Am. A* **33**, 1236 (2016).
  - [52] L.-G. Wang, *Opt. Express* **20**, 20814 (2012).
  - [53] J. P. Barton, D. R. Alexander, and S. A. Schaub, *J. Appl. Phys.* **66**, 4594 (1989).
  - [54] V. Kumar, G. M. Philip, and N. K. Viswanathan, *J. Opt.* **15**, 044027 (2013).
  - [55] E. J. Galvez, B. L. Rojec, V. Kumar, and N. K. Viswanathan, *Phys. Rev. A* **89**, 031801 (2014).
  - [56] R. Gutiérrez-Cuevas and M. A. Alonso, *Opt. Lett.* **42**, 2205 (2017).
  - [57] R. Gutiérrez-Cuevas and M. A. Alonso, *J. Opt. Soc. Am. A* **34**, 1697 (2017).